Electronic Supplementary Material (ESI) for Inorganic Chemistry Frontiers.

Electronic Supplementary Information (ESI)

Molecular-salt hybrids; integration of ammonia borane into lithium halides.

Irene Cascallana-Matías,[a,b] Joachim Breternitz,[a,†] Annabelle Baker,[c] Hallam Davis,[a] Edmund J. Cussen,[b,‡] Duncan H. Gregory.[a*]

a. WestCHEM, School of Chemistry, University of Glasgow, Glasgow, G12 8QQ, UK.
b. WestCHEM, Dept of Pure and Applied Chemistry, University of Strathclyde, Glasgow G1 1XL, UK.
c. Diamond Light Source, Harwell Oxford, Didcot, Oxfordshire OX11 0QX, UK.
†Present address: Energy Materials Division, Helmholtz Zentrum Berlin, Hahn-Meitner-Platz 1, 14109 Berlin, Germany.
‡ Present address: Dept of Chemical & Biological Engineering, University of Sheffield, Mappin Street, Sheffield S1 3JD, UK.

1. Full Experimental Details

All manipulations were performed in an MBraun LabSTAR argon-filled glovebox (>1 ppm O_2; >1 ppm H_2O).

Synthesis: $[LiBH_4]_2NH_3BH_3$ (**1**) and $Li(BH_3NH_2BH_2NH_2BH_3)$ (**2**) were synthesised following the previously reported procedures by Rush *et al* and Grochala *et al*, respectively.[1],[2] The LiI – NH_3BH_3 materials (**3** and **4**) were prepared from stoichiometric ratios of LiI (Sigma Aldrich, beads, 99%) and NH_3BH_3 (Sigma Aldrich, 98%). by ball milling (0.2 g powder) in hardened steel jars (50 ml) with 10 hardened steel balls of 10 mm diameter using a Retsch PM100 ball mill. The mixture was milled for 2 h at 250 rpm (400:1, ball-to-powder-ratio by mass). The ball milling was performed for periods of 2 min of milling interspersed by 2 min breaks to minimise overheating. The resultant products, both white in colour, were collected for characterisation.

Crystal structure analysis: Powder X-ray diffraction (PXD) data were obtained at room temperature with a Bruker D8 Advance (θ-2θ) diffractometer, using Cu Kα1 radiation and a step size of 0.017 º 2θ over an angular range 5-95 º 2θ for ca. 12 h. Experimental diffraction data were compared to powder patterns generated from data in the Inorganic Crystal Structure Database (ICSD) using PowderCell 2.4.[3] All data were indexed and refined by least squares fitting when possible using the CELREF software package.[4] Jana2006 was used for an initial Le Bail fitting and to assign the space group.[5] The structures of the new compounds **3** and **4** were then solved using Jana's interface to Superflip with the most promising cell candidates. For **4**, Jana2006 suggested two different options for the crystal system, either triclinic or monoclinic. A monoclinic structure was selected as the option of higher symmetry.

The possible space groups were *C*2/*m*, *Cm* or *C*2, since they bear the same translation symmetry. Given *C*2/*m* is the centrosymmetric space group, it was the first choice. However, refinements in this space group produced a triangular electron density around the mirror plane in the (020) plane. Since no meaningful atomic distances could be fitted to this electron density using a distorted *AB* model, it became evident that *C*2/*m* could not be the correct space group and that the triangular electron density was caused by incorrect assignment of symmetry. When the atoms were located in their correct sites, it was possible to observe that the mirror plane could not exist, confirming that the *C*2 space group is a better choice than *C*2/*m*. For both **3** and **4**, the B and N positions were exchanged to determine if a better fit could be obtained, however high positive and negative U_{iso} values respectively were observed for N and B. Li positions were tentatively identified from difference Fourier maps. High Resolution synchrotron PXD experiments were performed using beamline I11 (λ=0.826281(10) Å) at the Diamond Light Source to obtain improved descriptions of the structures derived from our original lab PXD models. The room temperature structures were refined against the synchrotron data using the Rietveld method as implemented in the GSAS software package via the EXPGUI interface.[6] The background was fitted using a shifted Chebyschev polynomial. The unit cell parameters were refined followed by the peak profile parameters, atomic positions and isotropic displacement parameters. The B–H and N–H bonds were restrained to values appropriate for tetrahedral species and the displacement parameters for the hydrogen atoms were fixed to be 1.2 times larger than those of the respective B and N atoms to which they were bonded.

Raman spectroscopy: Raman spectra were measured at room temperature using a Horiba Jobin Yvon Raman microscope with a green laser (λ=532 nm). A hole aperture of 50 μm, 100 g mm^{-1} grating and a synapse CCD detector were employed. Sealed glass capillaries were used to contain samples and thereby prevent air/moisture exposure during spectroscopic analysis.

Scanning electron microscopy (SEM) analysis: Sample morphology and composition were studied using SEM (XL 30 ESEM, Philips, 25 kV accelerating voltage). An Oxford Instruments X-act spectrometer was coupled to this microscope for EDX analysis. The instrument was calibrated using the INCA EDX analysis software (Cu used for all calibration measurements), which also allows selection of regions for analysis and definition of measurement parameters.

Thermal analysis: Thermogravimetric-differential thermal analysis (TG-DTA) was performed using a NETZSCH STA 409PC instrument coupled to a HIDEN HPR20 mass spectrometer (MS) for evolved gas analysis. Samples were placed in an alumina pan and heated from room temperature to 473 K at 5 K min-1 under an Ar flow. MS signals from H_2 (m/z = 2), NH_3 (m/z = 17), diborane (B_2H_6, m/z = 26-28), borazine ($B_3H_6N_3$, m/z = 80), H_2O (m/z = 18) and Ar (m/z = 40) were monitored as a function of time and temperature.

Ionic conductivity: Electrochemical impedance measurements were performed on cylindrical sample pellets of 13 mm diameter and 1−2 mm thickness that had been formed by pressing at room temperature under a load of 1 tonne for 20 min. A platinum paste was applied to opposite faces of the pellet to make electrical contacts. Data were collected on heating, and the temperature of the system was allowed to equilibrate for at least 1 h before every data collection. Data were collected using a

Solartron 1260 impedance analyser and were analysed using equivalent circuit analysis as implemented in the ZView2 software package.

2. SEM results

SEM images (**Figure S1**) show that **1** and **4** both possess a fused plate-like morphology, with individual plates measuring of the order of tens or hundreds of microns across. Images of **3** show that the material also forms an aggregate, but that the individual constituent particles appear far smaller (typically ≤10 microns). By contrast **2** has a sheet-like structure reminiscent of *AB*.

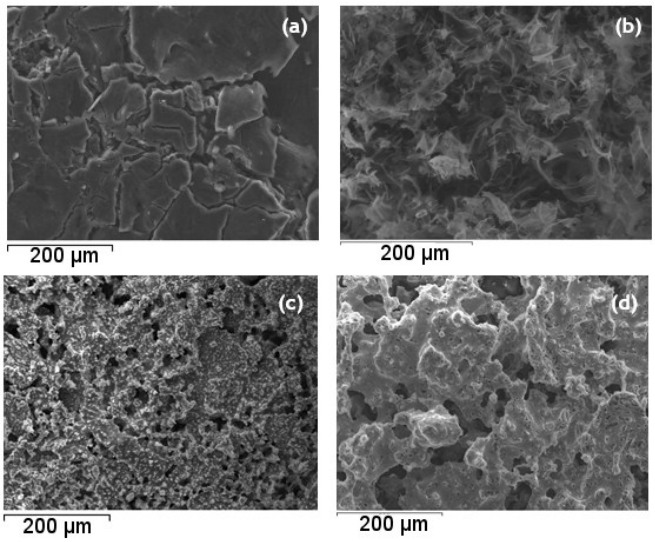

Figure S1. SEM images of synthesised materials: (a) $[LiBH_4]_2[NH_3BH_3]$ (**1**), (b) $Li(BH_3NH_2BH_2NH_2BH_3)$ (**2**), (c) $[LiI][NH_3BH_3]$ (**3**), and (d) $[LiI][NH_3BH_3]_2$ (**4**).

3. Characterisation of $[LiBH_4]_2[NH_3BH_3]$ (1)

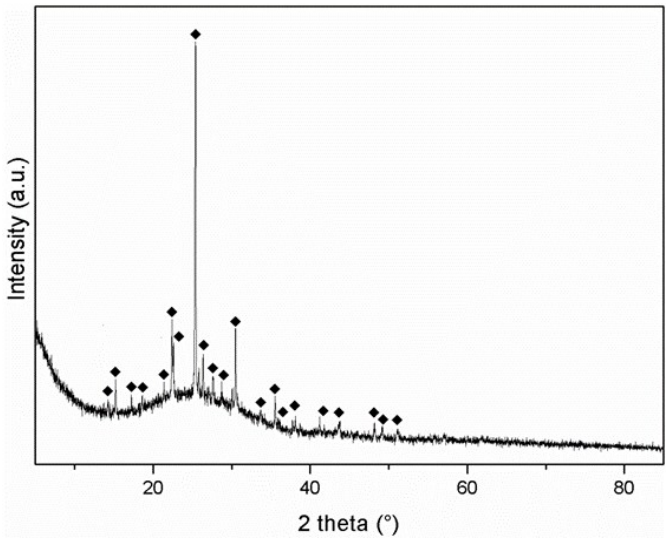

Figure S2. PXD pattern of the $LiBH_4$: NH_3BH_3 (2:1) reaction product: after 2 h ball milling (250 rpm, 400:1 ball-to-powder-ratio). Black diamonds represent $[LiBH_4]_2[NH_3BH_3]$ (**1**)**.**

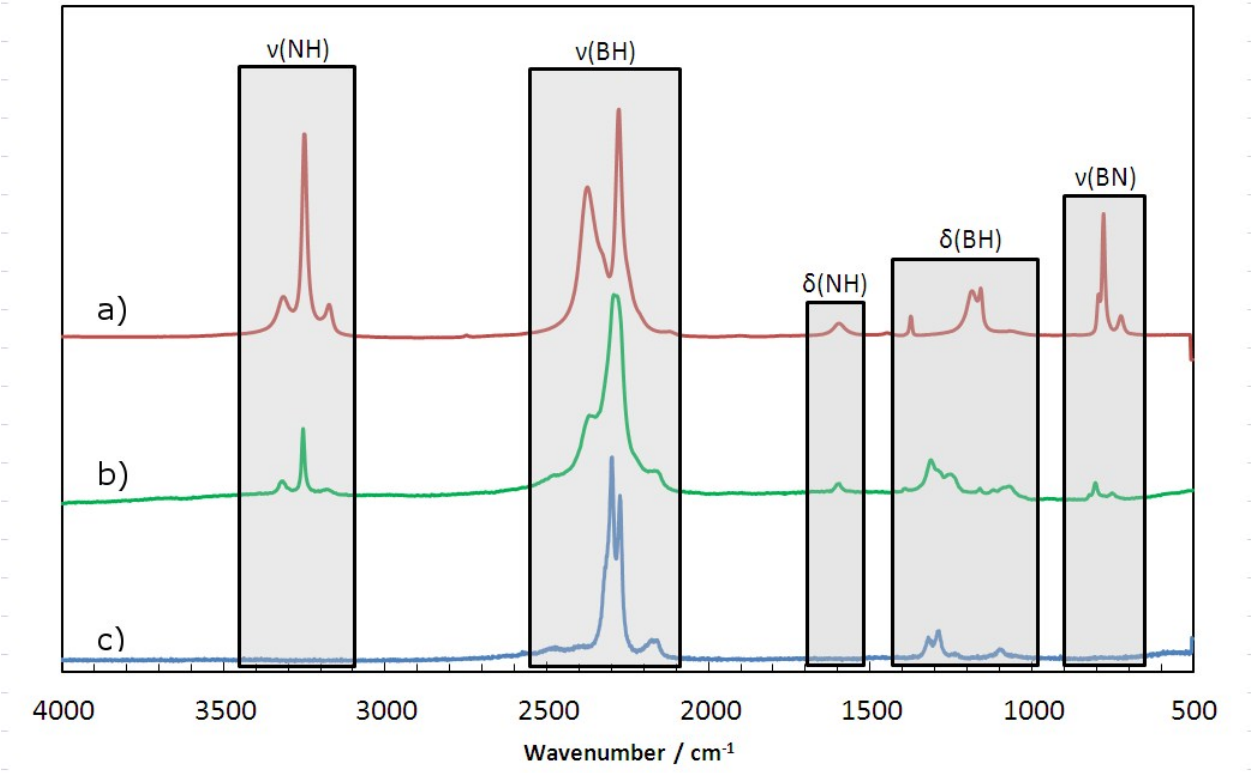

Figure S3. Raman spectra of (a) NH_3BH_3, (b) **1** and (c) $LiBH_4$, (ν = stretching, δ = deformation: bending and torsional modes).

$[LiBH_4]_2[NH_3BH_3]$ (**1**) loses 27.4 % of mass on heating to 200 ºC (**Figure S4**); MS results show that this mass loss is due to release of H_2, $B_3H_6N_3$ and B_2H_6 and NH_3 (**Figure S5**). The small weight loss at 112 ºC was observed previously in the literature and could be due to ammonia borane decomposing into $(NH_2BH_2)_n$.[1] There are no previous DTA data reported in the literature for $[LiBH_4]_2[NH_3BH_3]$.

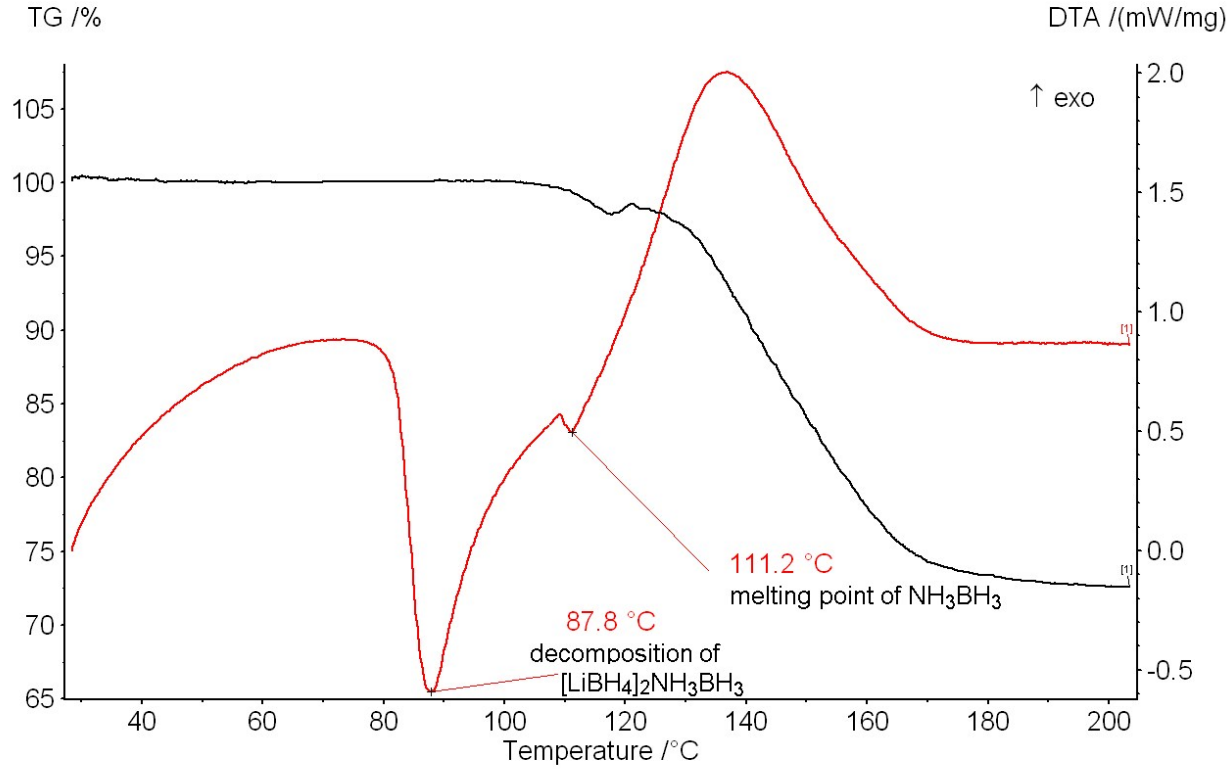

Figure S4. TG-DTA profile of **1** carried out in an Ar atmosphere, heating at 5 °C min^{-1} from ambient temperature to 200 °C. The black line represents the TG curve and the red line reprents the DTA curve.

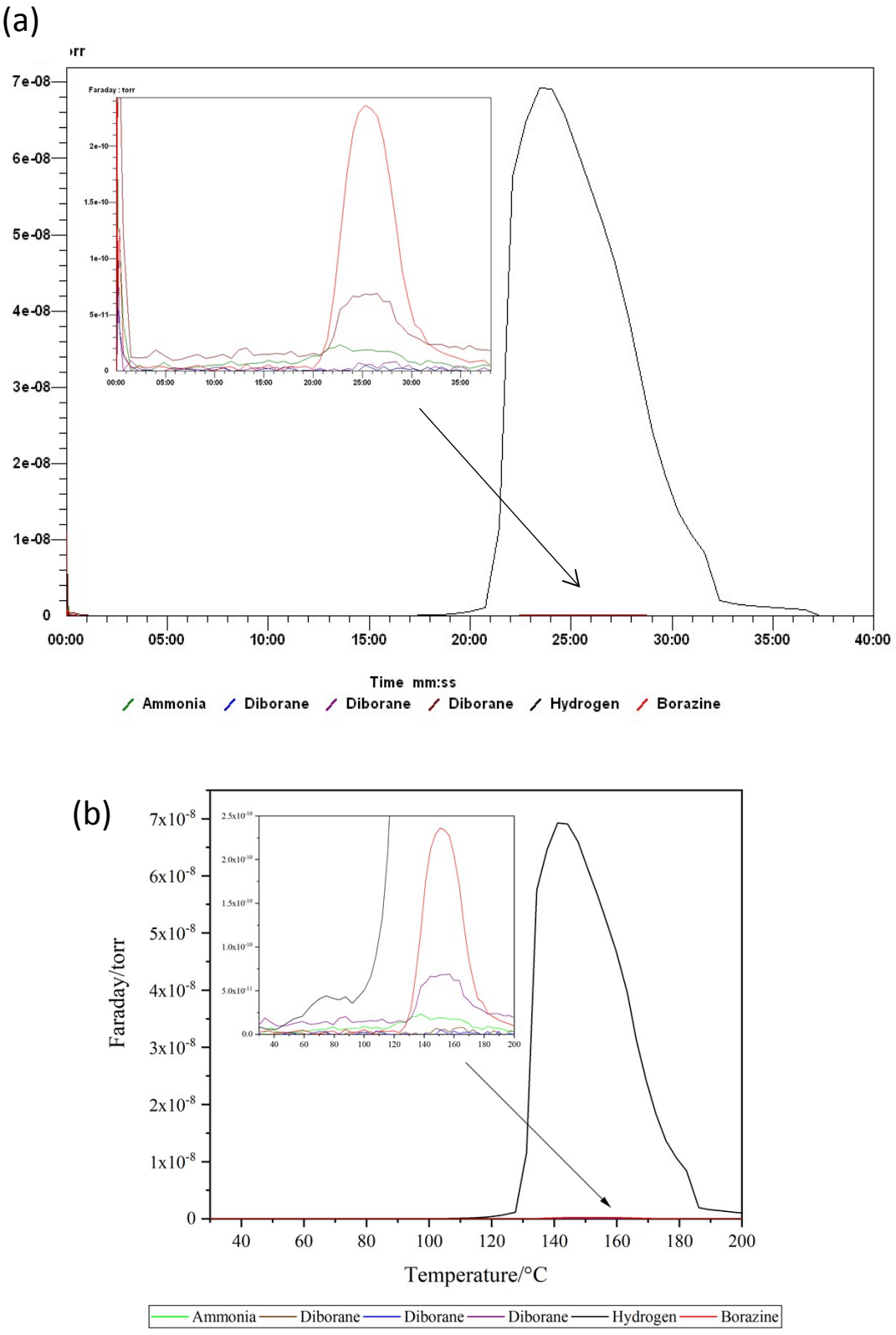

Figure S5. Evolved gas mass spectra for **1**. Gases monitored were: NH_3 (green); B_2H_6 (brown, blue and purple); $B_3H_6N_3$ (red); H_2 (black); (a) spectra vs time; (b) spectra vs temperature.

The PXD pattern of **1** post TG-DTA shows the formation of LT – $LiBH_4$ (**Figure S6**), suggesting that the mass loss originates mainly from the NH_3BH_3 component. No presence of HT – $LiBH_4$ was observed in the post TG-DTA PXD pattern, which is not unexpected since HT $LiBH_4$ is not stable at ambient temperature.[7]

The Raman spectrum of **1** after decomposition is shown in **Figure S7**. Ammonia borane normally decomposes into polyaminoborane $(NH_2BH_2)_n$ and polyiminoborane $(NHBH)_n$, however only polyiminoborane was detected from its characteristic peak at 3434 cm^{-1} corresponding to the υ(NH) mode. No peak from the $\upsilon(NH_2)$ mode at 3250 cm^{-1} from polyaminoborane was present.[8] Therefore the decomposition of **1** likely forms LT - $LiBH_4$ and $(NHBH)_n$ at 200 °C releasing H_2, NH_3, B_2H_6, and $B_3H_6N_3$ in the process.

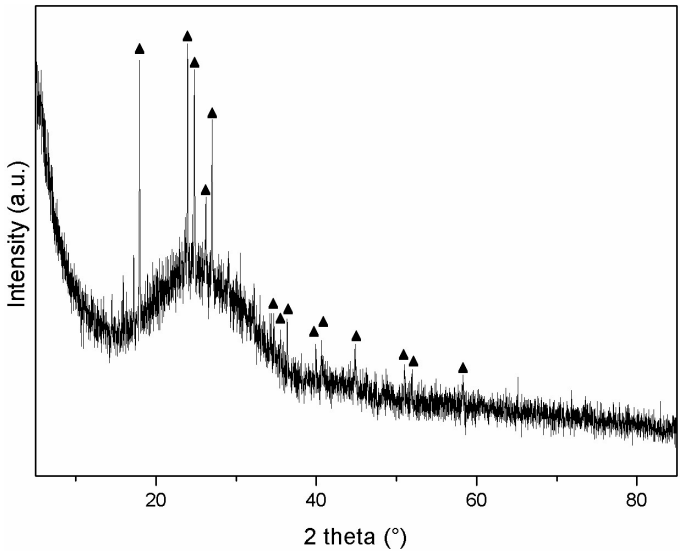

Figure S6. Post-TGA product after heating **1** under Argon from room temperature to 200 °C at 5 °C min^{-1}. Black triangles represent LT – $LiBH_4$.

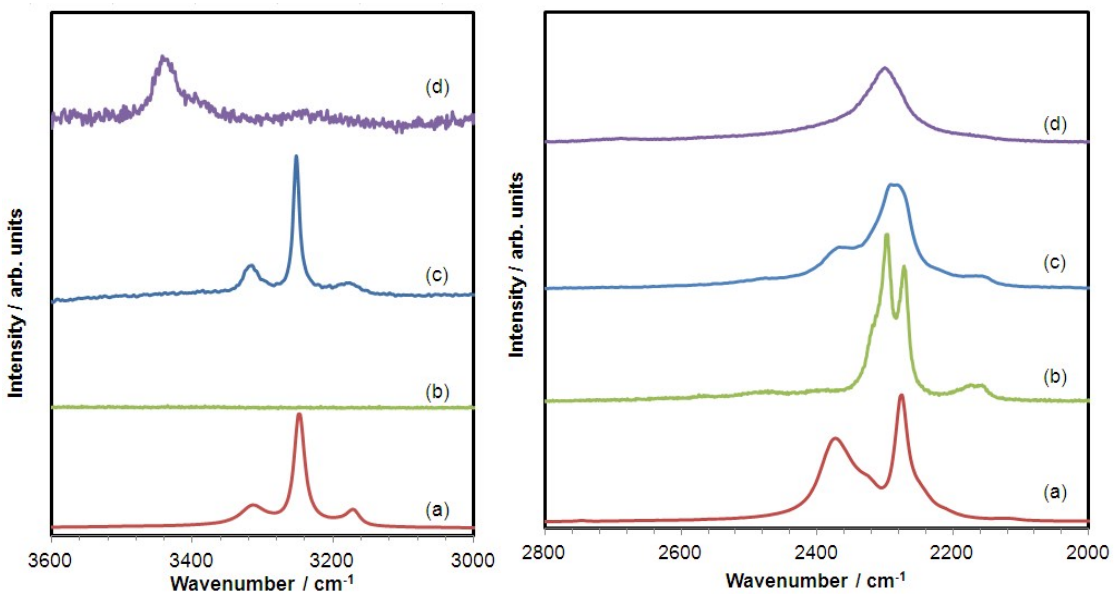

Figure S7. Raman spectra from 3000 - 3600 cm^{-1} (left) and from 2000 - 2800 cm^{-1} (right) of: (a) NH_3BH_3, (b) $LiBH_4$ and **1** (c) pre- and (d) post-TGA after heating under Argon from room temperature to 200 °C at 5 °C min^{-1}.

Table S1. Probable decomposition pathway for **1**.[2],[9]

Decomposition pathway (up to 200 ºC)		Gas evolved (wt. %)	Eqn.
$[LiBH_4]_2[NH_3BH_3]_{(s)}$	$\rightarrow$ 2 $LiBH_{4(s)}$ + $(NH_3BH_3)_{(s)}$	---	(1.1)[1]
	$\rightarrow$ 2 $LiBH_{4(s)}$ + 1/n $(NH_2BH_2)_{n\,(s)}$ + $H_{2(g)}$	2.7	(1.2)[1]
	$\rightarrow$ 2 $LiBH_{4(s)}$ + 1/n $(NHBH)_{n\,(s)}$ + 2 $H_{2(g)}$	5.4	(1.3)[1]
	or 2 $LiBH_{4(s)}$ + 1/3 $B_3H_6N_{3(g)}$ + 2 $H_{2(g)}$	42.7	(1.4)[1]

4. Characterisation of $Li(BH_3NH_2BH_2NH_2BH_3)$ (2)

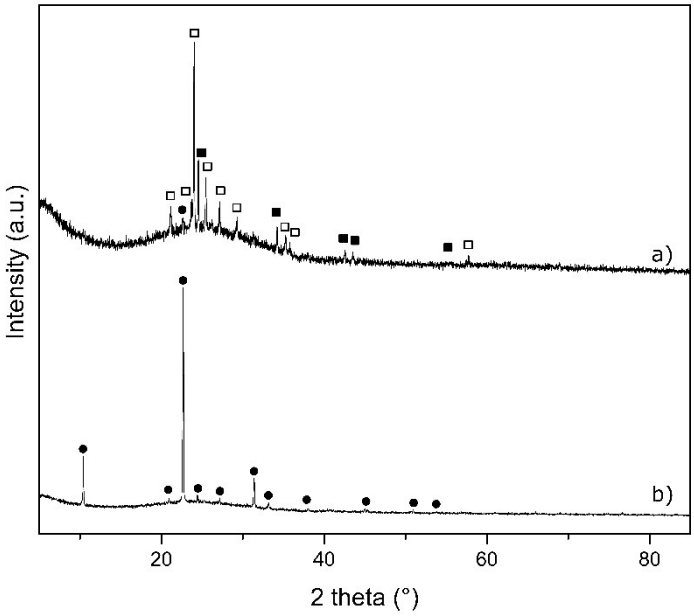

Figure S8. PXD pattern of a) LiH : NH_3BH_3 (1:3) reaction product post ball milling (2 h, ball to powder ratio 400:1) b) the LiH : NH_3BH_3 (1:3) reaction product post ball milling and thermal treatment at 75 °C. Open (white) squares represent $LiNH_2BH_3{\cdot}NH_3BH_3$; Closed (black) circles represent $Li(BH_3NH_2BH_2NH_2BH_3)$ (**2**); and closed (black) squares represent NH_3BH_3.

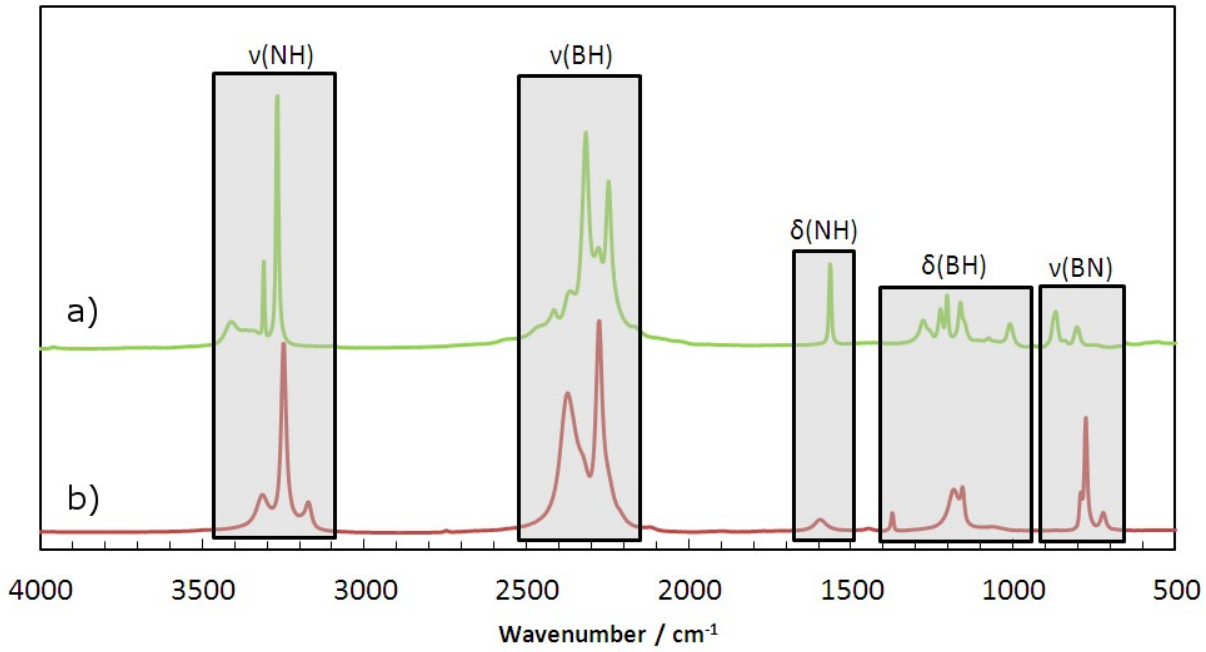

Figure S9. Raman spectra of (a) NH_3BH_3 and (b) **2** (ν = stretching, δ = deformation: bending and torsional modes).

TG-DTA data from **2** shows a total weight loss of 34% (**Figure S10**). A total loss of 10% wt.% is expected if **2** only follows equations (2.2) and (2.3) (reaction pathway (a) in **Table S2**) when heated to 200 °C. The higher observed weight loss could imply that **2** follows a rather different decomposition pathway below 200 °C. $LiBH_4$ and polymeric $(NHBH)_n$ (n=integer) might be expected as final products after the decomposition according to equation (2.2).[10] Evolved gas analysis shows the release of other gases in addition to H_2 such as $B_2H_6N_3$, B_2H_6 and NH_3 (**Figure S11**) which could suggest that **2** additionally follows reaction pathways (b) and/or (c) given by equations (2.4) and (2.5) in **Table S2** respectively. From Raman spectra $(NH_2BH_2)_n$ and $(NHBH)_n$ are tentatively identified from $\nu(NH_2)$ and $\nu(NH)$ bands, showing that complete decomposition of ammonia borane did not occur below 200 °C.[2],[8],[9] No Bragg reflections are observed in the PXD pattern (**Figure S12**) and the Raman band at 2296 cm^{-1} could originate from other polymeric BH_n-containing species or, in principle, correspond to the ν_1 (A_1) mode from (amorphous) $LiBH_4$ (**Figure S13**).

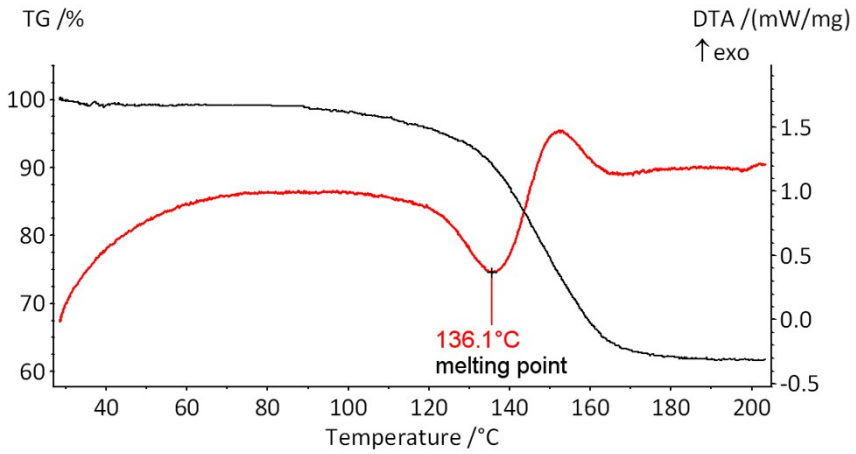

Figure S10. TG-DTA profile of **2** in an Ar atmosphere, heating at 5 °C min^{-1} from ambient temperature to 200 °C. The black line represents the TG curve and the red line reprents the DTA curve.

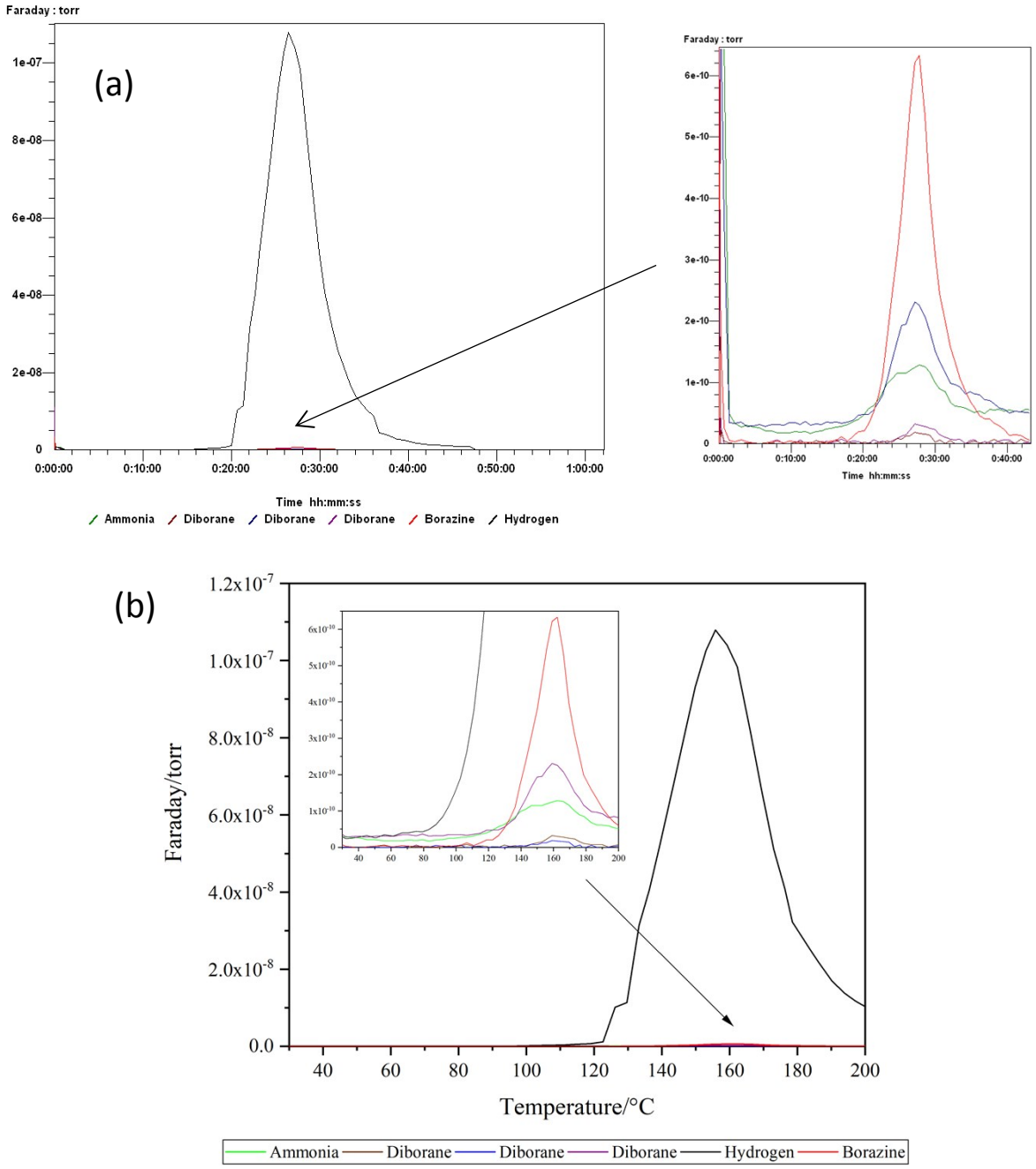

Figure S11. Evolved gas mass spectra for **2**. Gases monitored were: NH_3 (green); B_2H_6 (brown, blue and purple); $B_3H_6N_3$ (red); H_2 (black); (a) spectra vs time; (b) spectra vs temperature.

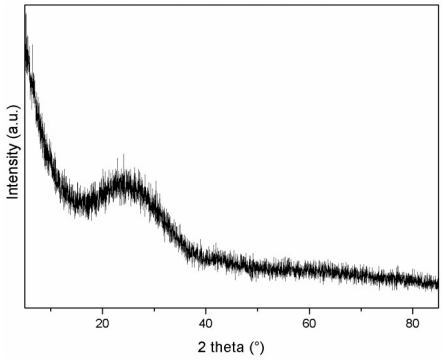

Figure S12. Post-TG-DTA product after heating **2** under an Argon flow from room temperature to 200 °C at 5 °C min^{-1}. No Bragg reflections could be identified or assigned.

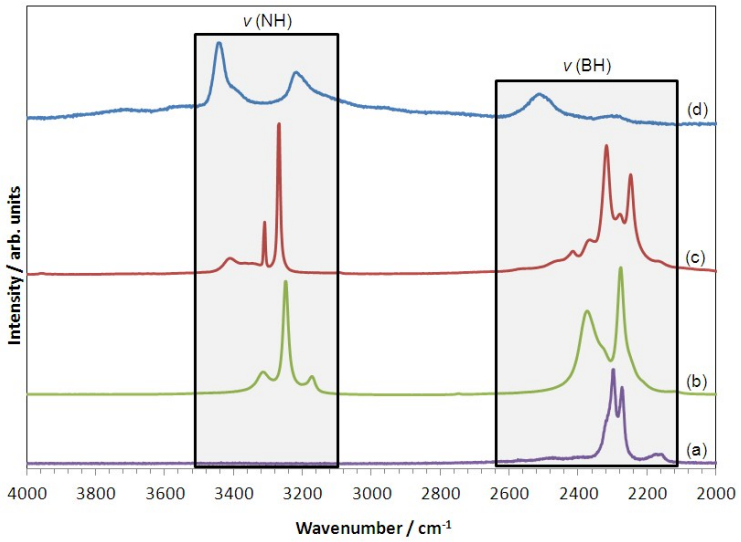

Figure S13. Raman spectra of (a) LT - $LiBH_4$, (b) NH_3BH_3 and (c) pre- and (d) post-TG-DTA of compound **2**.

Table S2. Possible decomposition pathways for **2.** (b) and (c) are theoretical proposed reactions and calculated weight losses.

Decomposition pathway				Calculated wt. % of gas evolved	Eqn.
(a)	$Li[BH_3NH_2BH_2NH_3BH_3]_{(s)}$	→	$LiBH_{4(s)} + 2/n\ (NH_2BH_2)_{n\ (s)}$	-	(2.1)
	$LiBH_{4(s)} + 2(NH_2BH_2)_{n\ (s)}$	→	$LiBH_{4(s)} + 2/n\ (NHBH)_{n\ (s)} + 2H_{2(g)}$	5.0 (H_2) (140 ºC)[2],[9]	(2.2)
	$LiBH_{4(s)} + 2(NHBH)_{n\ (s)}$	→	$LiBH_{4(s)} + 2BN_{(s)} + 2H_{2(g}$	5.0 (H_2) (200 ºC) [2],[9]	(2.3)
(b)	$Li[BH_3NH_2BH_2NH_2BH_3]_{(s)}$	→	$LiBH_{4(s)} + H_{2(g)} + 1/2B_2H_{6(g)} + NH_{3(g)} + BN_{(s)}$	41	(2.4)
(c)	$Li[BH_3NH_2BH_2NH_2BH_3]_{(s)}$	→	$LiBH_{4(s)} + 2/3B_3H_6N_{3(g)} + 2H_{2(g)}$	73	(2.5)

5. Characterisation of [LiI][NH_3BH_3] (3) and [LiI][NH_3BH_3]$_2$ (4)

Reactions performed in the LiI-NH_3BH_3 system are shown in **Table S3**. PXD patterns (**Figure S14**) show that when the LiI:*AB* ratio is increased to 2:1 excess LiI starting material appears as a secondary phase in the diffraction patterns. At intermediate LiI:*AB* ratios (e.g. 2:3), both the sets of reflections for **3** and **4** are visible suggesting that the two new iodide-*AB* phases coexist.

Table S3 Summary of reactions performed in the LiI-NH_3BH_3 system.

Reaction	Molar ratio LiI : NH_3BH_3	Products by PXD (**Figure S14**)
I	2:1	LiI, [LiI][NH_3BH_3] (**3**)
II	1:1	[LiI][NH_3BH_3] (**3**)
III	2:3	[LiI][NH_3BH_3] (**3**), [LiI][NH_3BH_3]$_2$ (**4**)
IV	1:2	[LiI][NH_3BH_3]$_2$ (**4**)

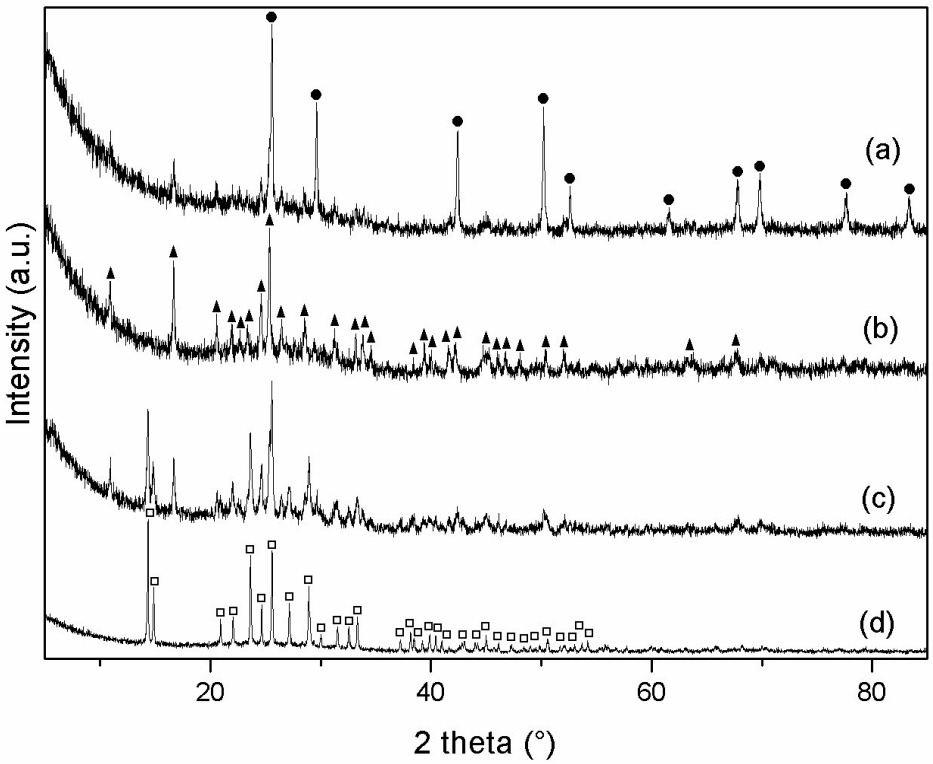

Figure S14. PXD patterns of the reaction products of LiI:NH_3BH_3 mixtures with ratios of: (a) 2:1; (b) 1:1; (c) 2:3 and (d) 1:2 . Filled circles represent LiI; Filled triangles represent **3**; and open squares represent **4**.

Figure S15 shows the Raman spectra of **3** and **4** as compared to ammonia borane. Although bands in the N-H, B-H and B-N regions are very similar across sample, there are some subtle changes in the positions of the bands and new peaks in the Raman spectrum of **3** and **4** are observed. In general, the sharp triplet in the Raman spectra assigned to the symmetric N-H stretching modes appears at higher wavenumbers for *AB* and **4** phase than for **3**.[11] Simultaneously, the most intense B-H stretching band (1375 cm^{-1}) falls at slightly higher wavenumber for **3** compared to **4**. These features suggest that the N–H bonds are slightly stronger for **4** than for **3**, while the opposite holds true for the B–H bonds. The B-N bands are observed at higher wavenumbers for **3** and **4** compared to *AB*. This might imply bonding of *AB* to Li through H–B. As determined by Rietveld refinement, the B–N bond length in **4** (1.542(24) Å) is shorter than that in **3** (1.580(6) Å) and both are shorter than the B-N distance in *AB* itself (1.597(3) Å).[12] One sharp band appearing for the HNH bending vibration at 1571 cm^{-1} is seen in the Raman spectrum of **3** and **4**; the presence of a single band suggests that the NH_3 groups have identical local symmetry.[2] Two weak N-B-H rocking bands are observed for *AB* at 726 and 1066 cm^{-1}, respectively.[11] The low and high frequency N-B-H rocking modes split into a doublet for both **3** and **4** potentially implying a reduction in molecular symmetry. Further analysis and modelling of the vibrational spectra will be performed in due course.

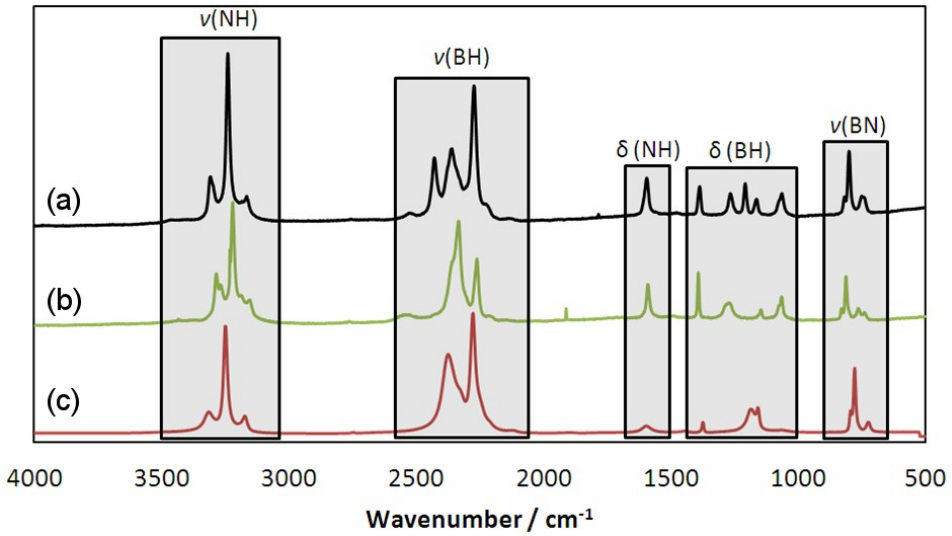

Figure S15. Raman spectra of (a) $[LiI][NH_3BH_3]_2$ (**4**), (b) $[LiI][NH_3BH_3]$ (**3**), and (c) NH_3BH_3 (ν = stretching, δ = deformation: bending and torsional modes).

The thermal stability of **3** and **4** was studied prior to performing the ionic conductivity experiments. $[LiI][NH_3BH_3]$ and $[LiI][NH_3BH_3]_2$ experience sharp endotherms at 119.5 °C and 114.2 °C respectively and both decompose exothermically in two steps thereafter (**Figure S16**). $[LiI][NH_3BH_3]$ begins to lose mass at 132.3 °C finally losing 11.9 wt.% on reaching 200 °C. TG-DTA-MS results show that this mass loss is due principally to the release of H_2 during the first weight loss of 2 wt. % at 132.3 °C and also to borazine ($B_3H_6N_3$), diborane (B_2H_6) and NH_3 in the second weight loss of 9.9 wt. % beginning at 144.2 °C (Figure S16). Theoretically, 4.2% of H_2 release would be expected if **3** decomposes following the same steps as ammonia borane (in the presence of LiI) (**Table S4**). $[LiI][NH_3BH_3]_2$ (**4**) begins to lose mass at 123.5 °C, which might again suggest the first step of the decomposition of ammonia borane (in the presence of LiI). The mass loss amounts to 2.7 wt. % before the 2nd decomposition step. At 143 °C another exothermic peak is observed, which is likely to arise from the further decomposition of ammonia borane, culminating in the loss of a further 13.82 wt. %.[8] Only 4.1 % of H_2 (**Table S5**) would be expected if **4** decomposes following the same path as ammonia borane (**Table S6**), however, **4** loses 16.52 % of mass on heating up to 200 ºC. TG-

DTA results show that the first mass loss is due to the release of H_2 and the second step is due to also $B_3H_6N_3$, B_2H_6 and NH_3 (Figure S16).

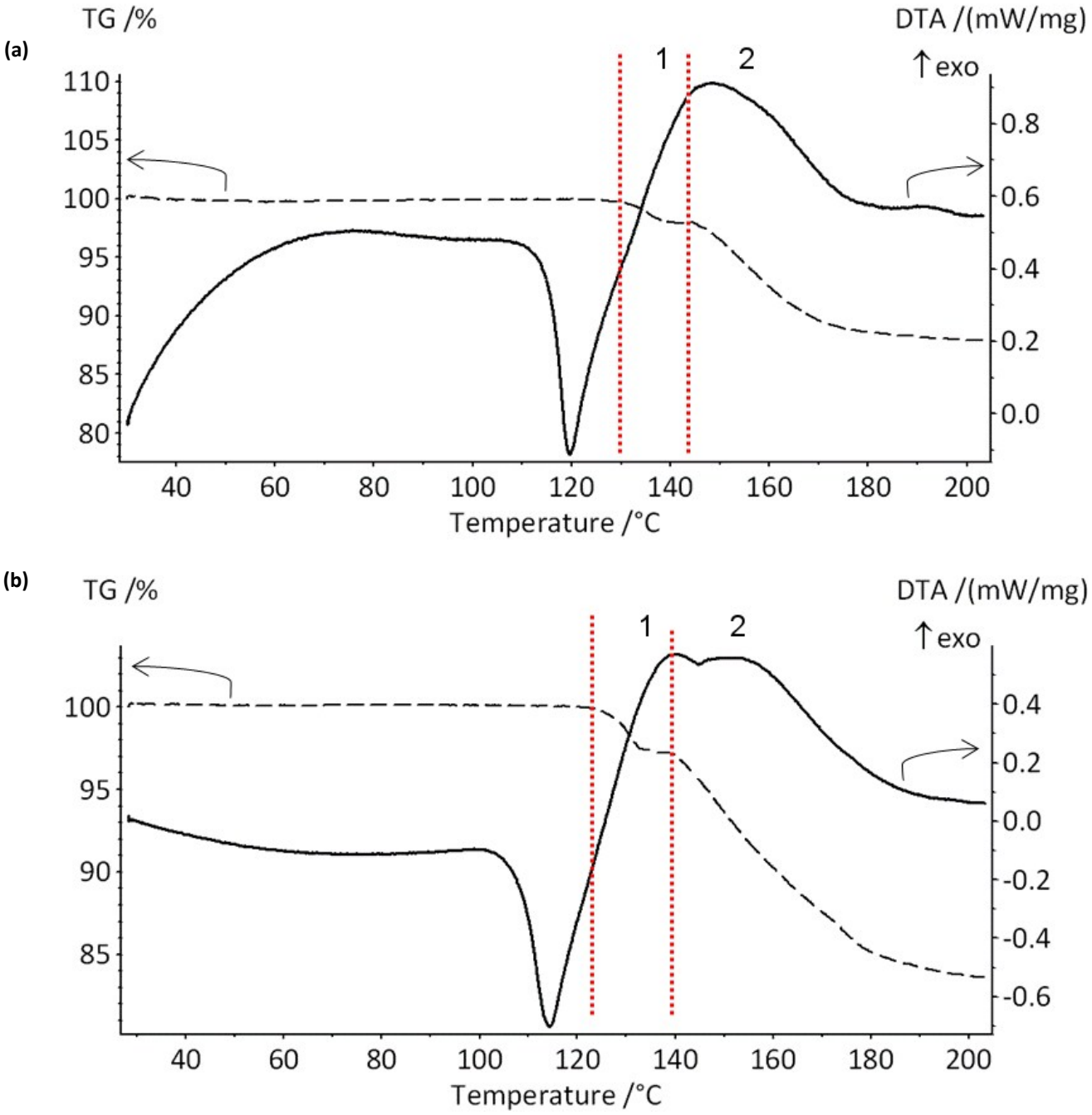

Figure S16. TG (solid lines) and DTA (dashed lines) profiles of (a) **3** and (b) **4** on heating at 5 °C min^{-1} under Ar from ambient temperature to 200 °C. The solid lines represent the TG curves and the dashed lines reprent the DTA curves. The red dotted lines define the onset temperatures of the first and second weight losses (marked "1" and "2").

Table S4. Possible decomposition pathways for $[LiI][NH_3BH_3]$ (**3**).

Decomposition pathway				Calculated wt. % of gas evolved	Eqn.
(a)	$[LiI][NH_3BH_3]_{(s)}$	→	$LiI_{(s)} + 1/2(NH_2BH_2)_{n\ (s)} + H_{2(g)}$	1.2 (H_2)	(3.1)
	$LiI_{(s)} + (NH_2BH_2)_{n\ (s)}$	→	$(NHBH)_{n\ (s)} + H_{2(g)}$	3.0 (H_2)	(3.2)
(b)	$[LiI][NH_3BH_3]_{(s)}$	→	$LiI_{(s)} + 1/2B_2H_{6(g)} + NH_{3(g)}$	18.7	(3.3)
(c)	$[LiI][NH_3BH_3]_{(s)}$	→	$LiI_{(s)} + 1/3B_3H_6N_{3(g)} + 2H_{2(g)}$	18.7	(3.4)

Table S5. Possible decomposition pathways for $[LiI][NH_3BH_3]_2$ (**4**).

Decomposition pathway				Calculated wt. % of gas evolved	Eqn.
(a)	$[LiI][NH_3BH_3]_{2(s)}$	→	$LiI_{(s)} + 2(NH_2BH_2)_{n\ (s)} + 2H_{2(g)}$	2.05 (H_2)	(3.5)
	$LiI_{(s)} + 2(NH_2BH_2)_{n\ (s)}$	→	$LiI_{(s)} + 2(NHBH)_{n\ (s)} + 2H_{2(g)}$	2.05 (H_2)	(3.6)
(b)	$[LiI][NH_3BH_3]_{2(s)}$	→	$LiI_{(s)} + B_2H_{6(g)} + 2NH_{3(g)}$	37.4	(3.7)
(c)	$[LiI][NH_3BH_3]_{2(s)}$	→	$LiI_{(s)} + 2/3B_3H_6N_{3(g)} + 4H_{2(g)}$	37.4	(3.8)

Table S6. Possible decomposition pathways for NH_3BH_3.

Decomposition pathway				Gas evolved (wt. %)	Eqn
(a)	$NH_3BH_{3(s)}$	→	$1/2(NH_2BH_2)_{n\ (s)} + H_{2(g)}$	6.4 (H_2)	(3.9)
	$(NH_2BH_2)_{n\ (s)}$	→	$(NHBH)_{n\ (s)} + H_{2(g)}$	6.6 (H_2)	(3.10)
(b)	$NH_3BH_{3(s)}$	→	$1/2B_2H_{6(g)} + NH_{3(g)}$	100	(3.11)
(c)	$NH_3BH_{3(s)}$	→	$1/3B_3H_6N_{3(g)} + 2H_{2(g)}$	100	(3.12)

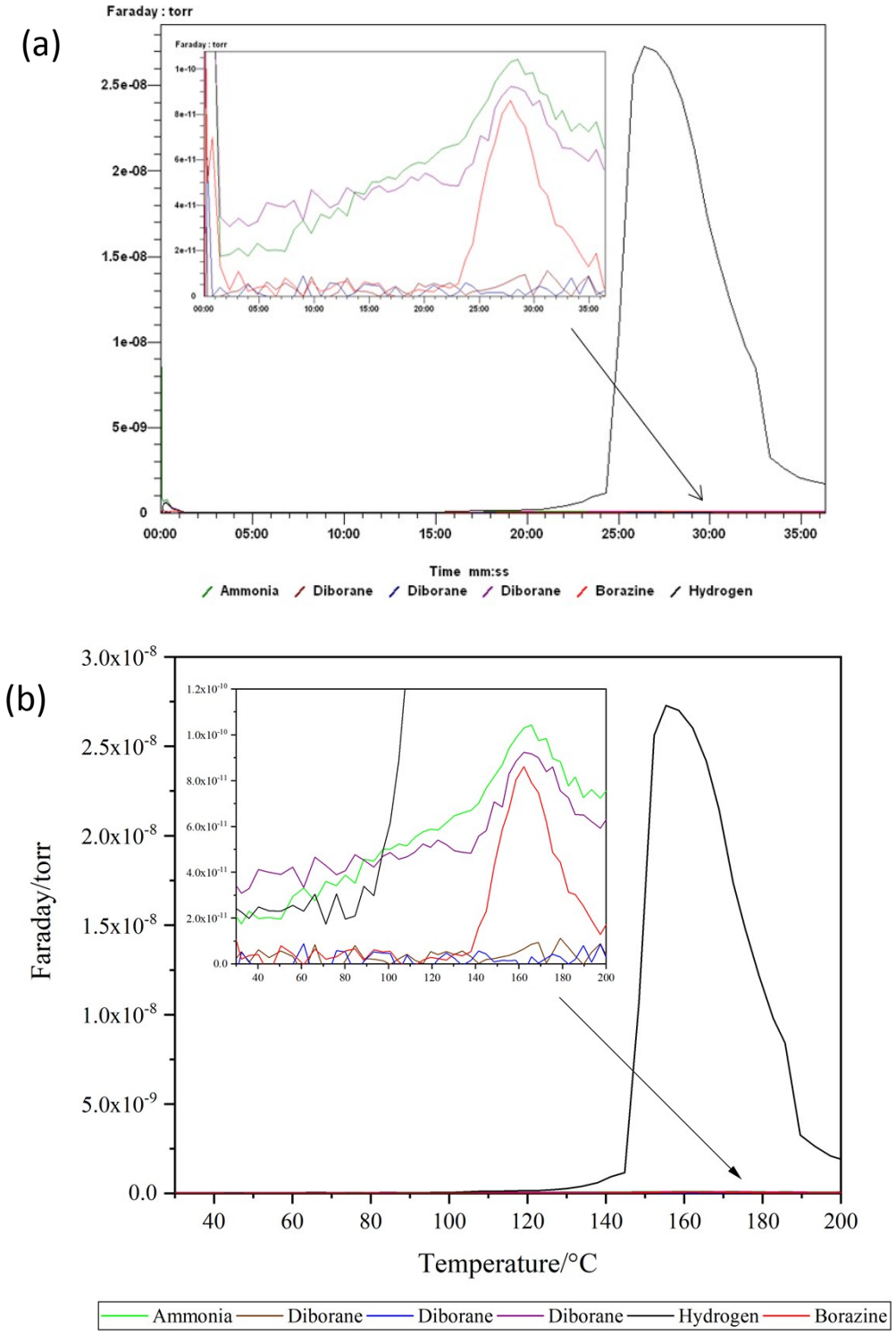

Figure S17. Evolved gas mass spectra recorded from **3**. Gases monitored were: NH_3 (green); B_2H_6 (brown, blue and purple); $B_3H_6N_3$ (red); H_2 (black); (a) spectra vs time; (b) spectra vs temperature.

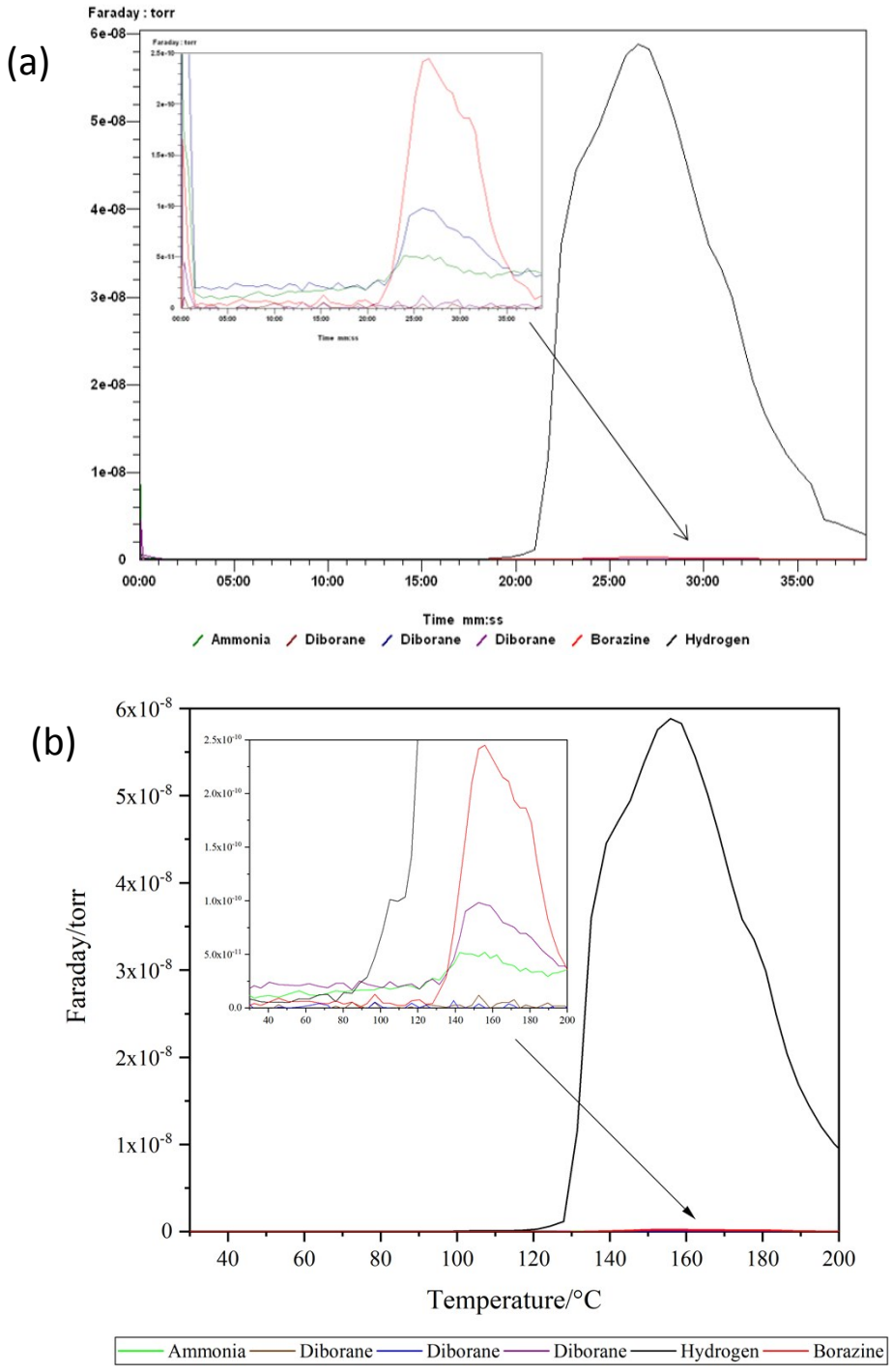

Figure S18. Evolved gas mass spectrum recorded for **4**. Gases monitored were: NH_3 (green); B_2H_6 (brown, blue and purple); $B_3H_6N_3$ (red); H_2 (black); (a) spectra vs time; (b) spectra vs temperature.

PXD patterns of **3** and **4** post-TG-DTA show the formation of polycrystalline LiI and probable amorphous content in each case (**Figure S19** and **Figure S20**), suggesting that the observed exothermic processes are associated with NH_3BH_3 decomposition.

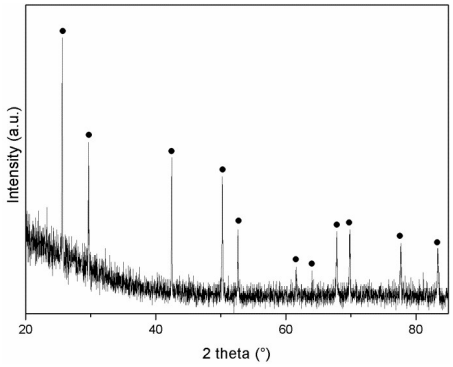

Figure S19. Post-TG-DTA product after heating **3** under argon from room temperature to 200 °C at 5 °C min^{-1}. Black circles represent LiI.

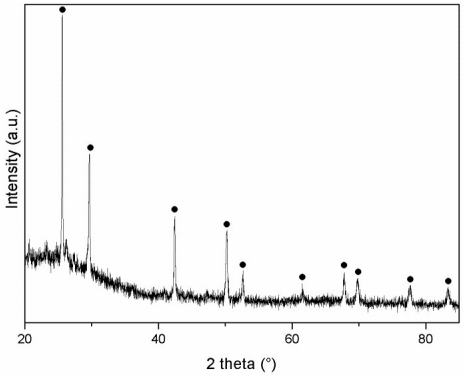

Figure S20. Post-TG-DTA product after heating **4** under argon from room temperature to 200 °C at 5 °C min^{-1}. Black circles represent LiI.

The post-TG-DTA Raman spectrum of **3** is shown in **Figure S21**. The ammonia borane component in **3** would be expected to decompose into polyaminoborane $(NH_2BH_2)_n$ and polyiminoborane $(NHBH)_n$ and signature bands from these species were detected at 3434 cm^{-1} (ν(NH) mode) and 3250 cm^{-1} (ν(NH_2) mode).[8] Therefore the decomposition of [LiI][NH_3BH_3] (**3**) likely results in the formation of LiI, NH_2BH_2 and NHBH releasing H_2, B_2H_6, $B_3H_6N_3$ and NH_3 (Figure S19, Figure S21 and Table S4).

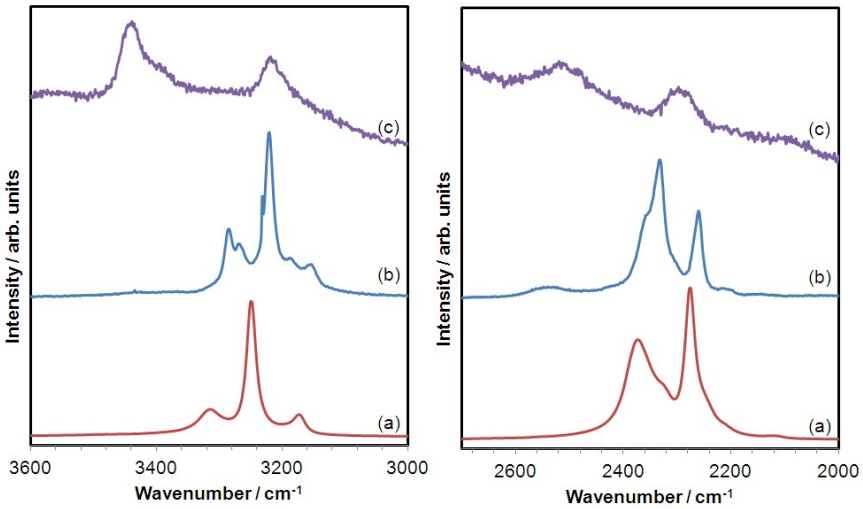

Figure S21. Raman spectra in the range of 3000 - 3600 cm^{-1} (left) and 2000 - 2800 cm^{-1} (right) of (a) NH_3BH_3 and **3** (b) pre- and (c) post-TG-DTA.

The Raman spectrum of **4** after decomposition is shown in **Figure S22**. It would be expected that the ammonia borane component decomposes into polyaminoborane $(NH_2BH_2)_n$ and polyiminoborane $(NHBH)_n$, but only bands corresponding to $(NHBH)_n$ were detected (dominated by the ν(NH) mode at 3434 cm^{-1}).[8] From PXD and Raman data the decomposition of $[LiI][NH_3BH_3]_2$ leads to LiI and $(NHBH)_n$ releasing H_2, B_2H_6, $B_3H_6N_3$ and NH_3 (**Table S5**, **Figure S20** and **Figure S22**).

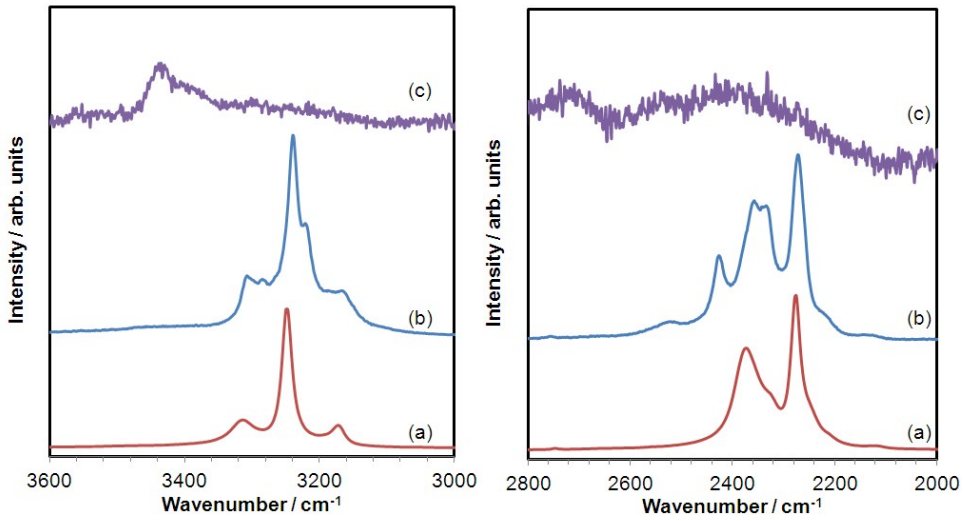

Figure S22. Raman spectra in the range 3000 - 3600 cm^{-1} (left) and 2000 - 2800 cm^{-1} (right) for (a) NH_3BH_3 and **4** (b) pre- and (c) post-TG-DTA after heating under argon from room temperature to 200 °C at 5 °C min^{-1}.

The I11 high-resolution synchrotron PXD data for **3** indicate a highly crystalline powder. However, two other minor phases were observed in the sample, NH_4I and $[LiI][NH_3BH_3]_2$ (**Figure S23**), which were not observed in the laboratory XRD data (which is surprising given the high scattering from I under X-rays). This could be due to the fact that the compound partially decomposed during handling/under the beam.

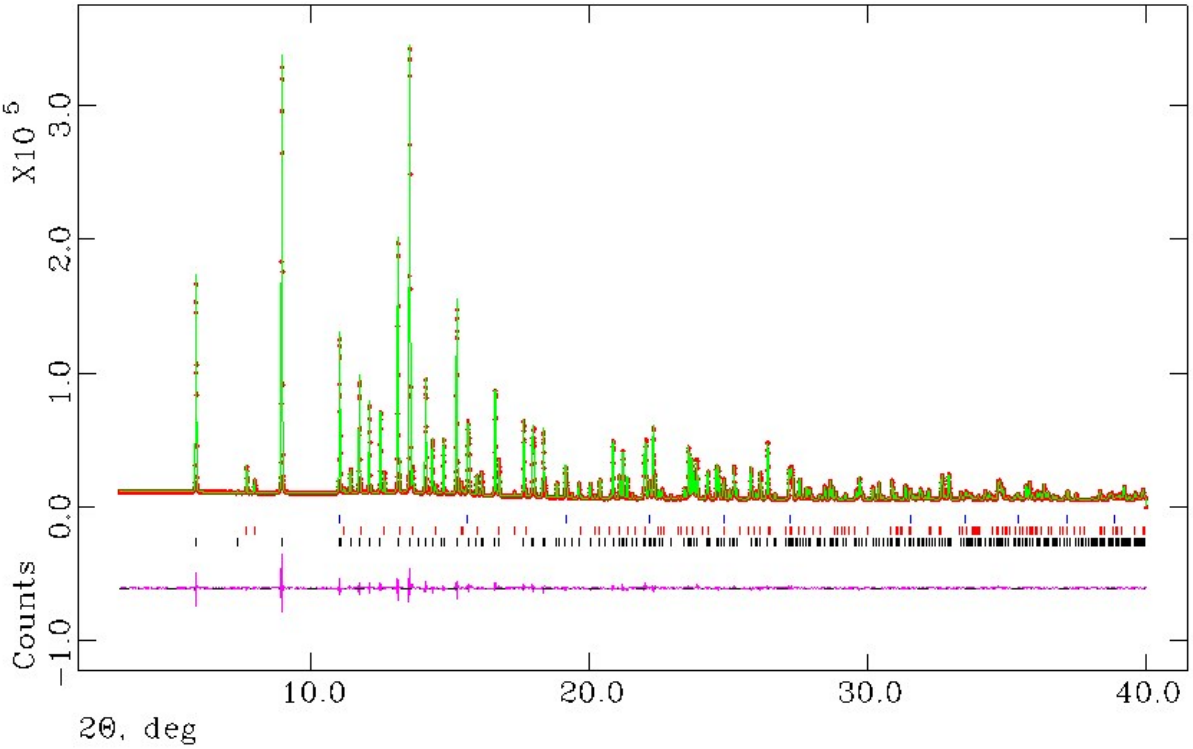

Figure S23. Profile plot for **3** from the Rietveld refinement against high-resolution synchrotron diffraction data (red dots: experimental profile; green line: calculated profile; pink line: difference profile; tick marks: Bragg reflections for the NH_4I (top), $[LiI][NH_3BH_3]_2$ (middle) and $[LiI][NH_3BH_3]$ (bottom).

Table S7. Selected Rietveld refinement data from synchrotron PXD data for **3** at 292 K.

Sample	$[LiI][NH_3BH_3]$
Empirical formula	$[LiI][NH_3BH_3]$
Collection temperature / K	292
Crystal system	Monoclinic
Space group	$P12_1/c1$
Z	4
Unit cell formula weight, M_w	658.84
Calculated density, ρ / g cm^{-3}	2.197
Phase fractions / %	
$[LiI][NH_3BH_3]$	90(5)
$[LiI][NH_3BH_3]_2$	5(3)
NH_4I	5(3)
Unit cell dimensions:	
a / Å	4.39140(1)
b / Å	16.17291(5)
c / Å	7.15685(2)
β / °	101.52(2)
V / Å^3	498.0443(27)
Observations, parameters	9228, 82
R_{wp}	0.0336
R_p	0.0232

Table S8. Atomic positions and isotropic displacement parameters obtained from Rietveld refinement against synchrotron powder diffraction data for **3** at 292 K.

Atom	Site	SOF[a]	*x*	*y*	*z*	100 x U_{iso} / Å^2
Li	4*e*	1	0.884(22)	0.3232(6)	0.6490(13)	2.4(4)
I	4*e*	1	0.40873(9)	0.415344(24)	0.75230(6)	3.30(2)
N	4*e*	1	0.0561(8)	0.39268(23)	0.2134(6)	4.1(1)
B	4*e*	1	0.879(2)	0.31725(32)	0.2830(11)	2.6(2)
H1B	4*e*	1	0.7505	0.2866	0.1642	3.1(4)
H2B	4*e*	1	0.0168	0.7277	0.6360	3.1(4)
H3B	4*e*	1	0.6971	0.3427	0.3448	3.1(4)
H1N	4*e*	1	0.2460	0.1059	0.7866	4.9(2)
H2N	4*e*	1	0.0883	0.3810	0.1018	.4.9(2)
H3N	4*e*	1	0.9803	0.0591	0.7253	4.9(2)

[a] Site occupancy factor

The unit cell of [LiI][NH_3BH_3] (**3**) contains atoms that are all located on 4*e* general positions with 2 sets of 3 crystallographically-inequivalent H positions associated with the *AB* boron and nitrogen atoms respectively. In terms of the local structure, individual Li^+ cations could be considered to be tetrahedrally coordinated by two I^- anions and two *AB* molecules. However, the extended structure essentially comprises Li-I zig-zag chains that propagate along the [100] direction with *AB* connecting the chains approximately orthogonally. The shortest Li – I, Li – B and Li – Li distances are 2.718(9), 2.467(10) and 4.290(10) Å, respectively, while the B-N bond distance in **3** is 1.580(6) Å. This is slightly shorter than the equivalent distance in ammonia borane itself (1.597(3) Å),[12] the B-N distances in the previously reported structure of [$LiBH_4$]$_2$[NH_3BH_3] (**1** herein) and the alkaline earth ammonia borane borohydrides $Mg(BH_4)_2[NH_3BH_3]_2$ and $Ca(BH_4)_2[NH_3BH_3]_2$ (1.5960(1), 1.5906(1) and 1.5906(2) Å respectively).[1],[12]

The structure of [LiI][NH_3BH_3]$_2$ (**4**) consists of discrete ionic and molecular sections with pseudo-layers of *AB*, which are two molecules wide, stacked along the crystallographic *a*-axis. The atoms are located on 4*c* general positions, apart from I on 2*b*, with 2 sets of 3 crystallographically-inequivalent H positions associated with the *AB* boron and nitrogen atoms respectively. Placing the Li ion on the 4*c* site with 50% occupancy (as opposed to its location on the 2*a* (0, *y*, 0) site) produced a marginally better fit in the refinement and physically reasonable Li - B and Li - N interatomic distances. Lithium cations and iodide anions are situated in *a* plane (*i*.e. parallel to the *bc* plane) within the *AB* "interlayer" regions. As in **3**, Li^+ ions are pseudo-tetrahedrally coordinated by two I^- anions and two *AB* molecules. By comparison to **3**, the Li – I

bond distance in **4** is notably larger (2.796(31) Å), suggesting that Li^+ is less strongly bound with the ionic sublattice. The closest Li – Li distance is also longer in **4** (4.32(8) Å) than **3**. Li atoms from **4** are found to be closer to B than to N from the ammonia group, with Li – B and Li – N bond distances of 2.363(33) and 3.317(22) Å, respectively. However, Li atoms in **3** are relatively closer to B, with shorter bond distances. The B-N distance in **4** is 1.542(24) Å, which is slightly shorter than that in **3** but remains similar to the equivalent distance in lithium amidoborane, $Li[NH_2BH_3]$ (1.547 Å).[13]

Table S9. Selected interatomic distances for **3** from high-resolution synchrotron diffraction data at 292 K.

	Bond length / Å		Bond length / Å
B – N	1.580(6) x 1	Li – I	2.784(9) x 1
B – N	4.546(7) x 1	Li – I	2.718(9) x 1
B – Li	4.544(12) x 1	Li – I	4.993(9) x 1
B – Li	4.663(12) x 1	Li – N	4.437(10) x 1
B – Li	2.467(10) x 1	Li – N	3.534(10) x 2
B – Li	2.616(12) x 1	Li – N	4.115(9) x 1
Li – Li	4.39140(1) x 2	Li – N	4.696(9) x 1
Li – Li	4.290(10) x 2	Li – N	3.582(10) x 1

The high-resolution synchrotron diffraction data from **4** indicates that the powder was highly crystalline and single phase (**Figure S24**).

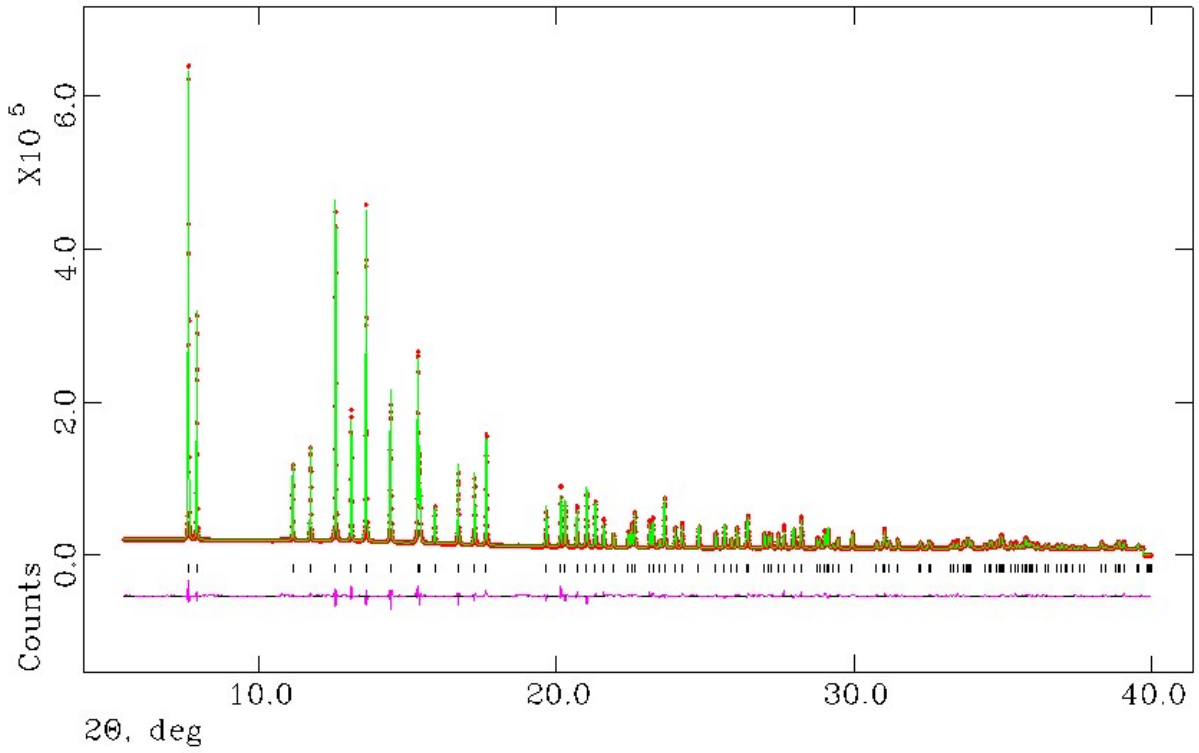

Figure S24. Profile plot from the Rietveld refinement against high-resolution synchrotron PXD data for **4** (red dots: experimental profile; green line: calculated profile; pink line: difference profile; tick marks: Bragg reflections for $[LiI][NH_3BH_3]_2$).

Table S10. Selected Rietveld refinement data from synchrotron PXD data for **4** at 292 K.

Sample	$[LiI][NH_3BH_3]_2$
Empirical formula	$[LiI][NH_3BH_3]_2$
Collection temperature / K	292
Crystal system	Monoclinic
Space group	*C*2
Z	2
Unit cell formula weight, M_w	391.15
Calculated density, ρ / g cm^{-3}	1.708
Unit cell dimensions:	
a / Å	12.40709(4)
b / Å	7.22117(3)
c / Å	4.42025(2)
β / °	106.21(1)
V / Å^3	380.275(2)
Observations, parameters	8687, 40
R_{wp}	0.0409
R_p	0.0269

Table S11. Atomic positions and isotropic displacement parameters obtained from Rietveld refinement against synchrotron PXD data for **4** at 292 K.

Atom	Site	SOF[a]	*x*	*Y*	*z*	100 x U_{iso} / Å^2
Li	4*c*	0.5	0.5274(25)	0.249(4)	0.038(8)	2.1(9)
I	2*b*	1	0.5	0.004(4)	0.5	3.98(3)
N	4*c*	1	0.1705(5)	0.141(4)	0.2160(14)	4.1(2)
B	4*c*	1	0.8463(6)	0.982(6)	0.0243(19)	8.1(4)
H1B	4*c*	1	0.7991	0.0124	0.1666	9.8(5)
H2B	4*c*	1	0.8315	0.8694	0.9183	9.8(5)
H3B	4*c*	1	0.9292	0.9955	0.1521	9.8(5)
H1N	4*c*	1	0.1218	0.1318	0.3185	5.0(3)
H2N	4*c*	1	0.2383	0.1262	0.3426	5.0(3)
H3N	4*c*	1	0.1664	0.2466	0.1219	5.0(3)

[a] Site occupancy factor

Table S12. Selected interatomic distances for **4** from high-resolution synchrotron data at 292 K.

	Bond length / Å
B – N	1.542(24) x 1
B – N	3.542(20) x 1
B – N	3.611(12) x 1
B – N	4.040(11) x 1
B – N	4.383(21) x 1
Li – Li	4.32(8) x 1
Li – Li	4.42025(2) x 2
Li – Li	4.61(7) x 1

	Bond length / Å
Li – N	3.317(22) x 1
Li – N	3.709(23) x 1
Li – I	2.796(31) x 1
Li – I	2.910(31) x 1
B – Li	2.790(33) x 1
B – Li	2.363(33) x 1
B – Li	4.34(4) x 1
B – Li	4.420(32) x 1

6. AC Impedance Data

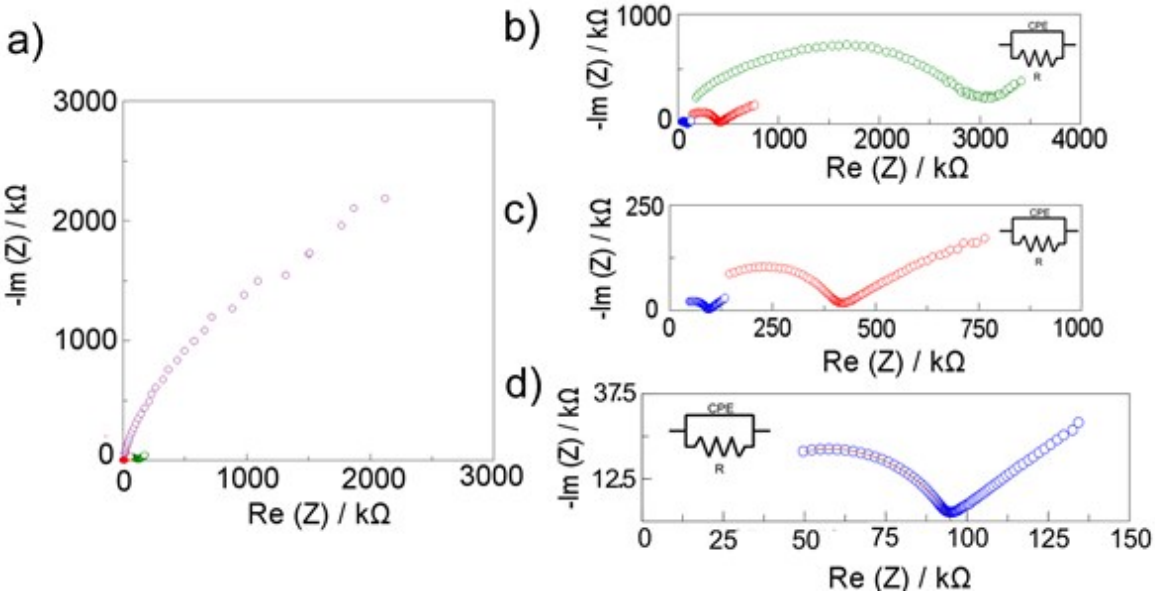

Figure S25. Ionic conductivities for **1**-**4**. Impedance plots at 292 K for: (a) **1**-**4**, (b) **1**, **3**, and **4**, (c) **1** and **4**, (d) **4** only. **1**-**4** are represented in red, magenta, green and blue respectively in all plots

7. References

[1] H. Wu, W. Zhou, F. E. Pinkerton, M. S. Meyer, G. Srinivas, T. Yildirim, T. J. Udovic, J. J. Rush, *J. Mater. Chem.* **2010**, *20*, 6550.

[2] K. J. Fijalkowski, T. Jaron, P. J. Leszczynski, E. Magos-Palasyuk, T. Palasyuk, M. K. Cyranski, W. Grochala, *Phys. Chem. Chem. Phys.* **2014**, *16*, 23340.

[3] W. Kraus, G. Nolze, *Powder Diffr.* **1998**, *13*, 256.

[4] J. Laugier, B. Bochu, CELREF: Cell parameters refinement program from powder diffraction diagram. Laboratoire des Matériaux et du Génie Physique, Ecole Nationale Supérieure de Physique de Grenoble (INPG), **1999**.

[5] V. Petricek, M. Dusek, L. Palatinus, *Z. Kristall.* **2014**, *229*, 345.

[6] a) A. C. Larson, R. B. Von Dreele, *General Structure Analysis System (GSAS), Los Alamos National Laboratory Report LAUR*, **1994**, 86-748; b) B. H. Toby, *J. Appl. Crystallogr.* **2001**, *34*, 210.

[7] J. P. Soulie, G. Renaudin, R. Cerny, K. Yvon, *J. Alloy. Compd.* **2002**, *346*, 200.

[8] R. S. Chellappa, T. Autrey, M. Somayazulu, V. V. Struzhkin, R. J. Hemley, *Chem. Phys. Chem.* **2010**, *11*, 93.

[9] R. Owarzany, K. J. Fijalkowski, T. Jaroń, P. J. Leszczyński, Ł. Dobrzycki, M. K. Cyrański, W. Grochala, *Inorg. Chem.* **2015**, *215*, 324.

[10] H. Chu, G. Wu, Z. Xiong, J. Guo, T. He, P. Chen, *Chem. Mat.* **2010**, *22*, 6021.

[11] N. J. Hess, M. E. Bowden, V. M. Parvanov, C. Mundy, S. M. Kathmann, G. K. Schenter, T. Autrey, *J. Chem. Phys.* **2008**, *128*, 034508.

[12] M. E. Bowden, G. J. Gainsford, W. T. Robinson, *Aust. J. Chem* **2007**, *60*, 149.

[13] H. Wu, W. Zhou, T. Yildirim, *J. Am. Chem. Soc.* **2008,** *130*, 14834.